

# Isotropic Iodide Adsorption Causes Anisotropic Growth of Copper Microplates

Myung Jun Kim,<sup>||</sup> Mutya A. Cruz,<sup>||</sup> Zihao Chen,<sup>||</sup> Heng Xu, Micah Brown, Kristen A. Fichthorn,<sup>\*</sup> and Benjamin J. Wiley<sup>\*</sup>

Cite This: *Chem. Mater.* 2021, 33, 881–891

Read Online

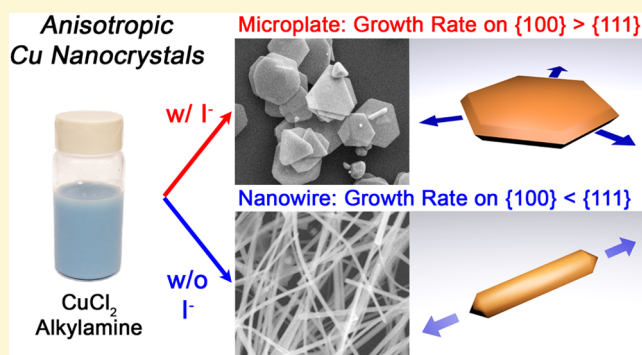
ACCESS |

Metrics & More

Article Recommendations

Supporting Information

**ABSTRACT:** Control over the shape of a metal nanostructure grants control over its properties, but the processes that cause solution-phase anisotropic growth of metal nanostructures are not fully understood. This article shows why the addition of a small amount (75–100  $\mu\text{M}$ ) of iodide ions to a Cu nanowire synthesis results in the formation of Cu microplates. Microplates are 100 nm thick and micronwide crystals that are thought to grow through atomic addition to {100} facets on their sides instead of the {111} facets on their top and bottom surfaces. Single-crystal electrochemical measurements show that the addition of iodide ions decreased the rate of Cu addition to Cu(111) by 8.2 times due to the replacement of adsorbed chloride by iodide. At the same time, the addition of iodide ions increased the rate of Cu addition to Cu(100) by 4.0 times due to the replacement of a hexadecylamine (HDA) self-assembled monolayer with the adsorbed iodide. The activation of {100} facets and passivation of {111} facets with increasing iodide ion concentration correlated with an increasing yield of microplates. Ab initio thermodynamics calculations show that, under the experimental conditions, a minority of iodide ions replaces an overwhelming majority of chloride and HDA on both Cu(100) and Cu(111). While Cu nanowire formation is predicted (and observed) in solutions containing chloride and HDA, the calculations indicate that a strong thermodynamic driving force occurs for {111} facet (and microplate) growth when a small amount of iodide is present, consistent with the experiment.



## INTRODUCTION

The development of colloidal syntheses to control the shape of metal nanocrystals has enabled the customization of their properties for different applications.<sup>1</sup> For example, increasing the coverage of certain crystal facets on nanocrystal surfaces can increase their catalytic performance.<sup>2–8</sup> The high aspect ratio of metal nanowires enables their use in transparent conductors,<sup>9,10</sup> highly porous felts,<sup>11</sup> aerogels,<sup>12–14</sup> and conductive composites.<sup>15–17</sup> Two-dimensional (2D) nanoplates and microplates exhibit size-dependent surface plasmon resonance (SPR)<sup>18</sup> that has been employed for photothermal therapy,<sup>19</sup> SPR biosensors,<sup>20</sup> and photoacoustic imaging.<sup>21</sup> Microplates can also be used to form conductive networks for printed electronics<sup>22–24</sup> and conductive polymer composites.<sup>25</sup> These examples demonstrate the power that morphological control of metal nanocrystals can provide for those seeking to understand structure–property relationships of metal nanomaterials and improve their performance in various applications.

The mechanisms by which shape control is achieved in solution-phase metal nanostructure syntheses are not well understood. This lack of fundamental understanding makes it difficult to design syntheses that produce the desired outcome.

A common hypothesis is that shape-directing agents preferentially adsorb to certain facets of a nanocrystal, altering the facet-dependent surface energy and kinetics of atomic addition.<sup>26–30</sup> Shape-directing agents may take the form of an ion, an organic compound, a polymer, or a gas (e.g., CO). Wulff constructions of face-centered cubic (fcc) metals predict that the thermodynamically favored structure is a truncated octahedron composed of both {111} and {100} facets.<sup>31</sup> The addition of certain capping agents can result in the synthesis of octahedra covered exclusively by eight {111} facets or nanocubes enclosed by six {100} facets.<sup>31</sup> Recent results suggest that the observed deviation in facet coverage can be due to a change in the facet-dependent kinetics of atomic addition rather than the facet-dependent surface energy.<sup>32–34</sup> Indeed, the highly anisotropic shape of nanowires seems to indicate that such structures must result from a change in the

Received: September 7, 2020

Revised: November 18, 2020

Published: December 7, 2020



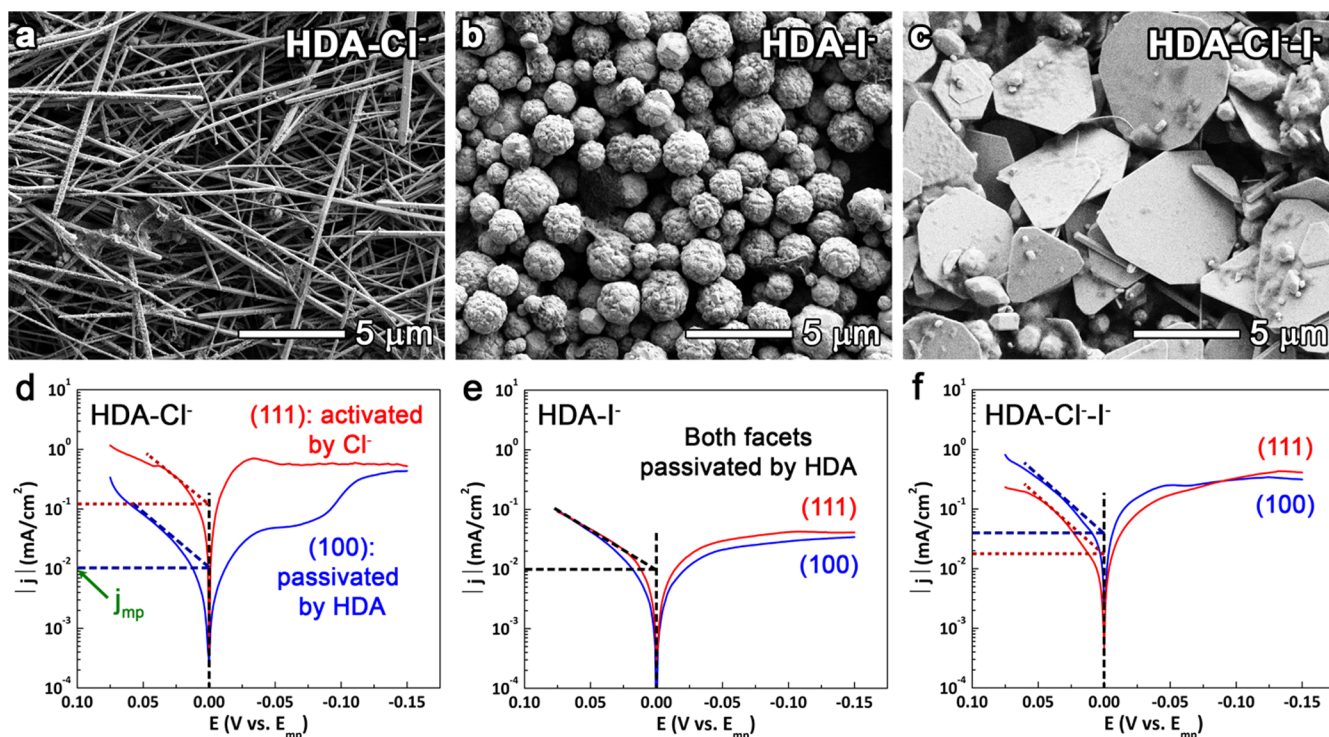


**Figure 1.** Cu nanostructures synthesized with HDA, AA, and different combinations of Cu precursors and halide ions: (a) nanowires formed with a  $\text{CuCl}_2$  precursor, (b) spherical particles formed with  $\text{Cu}(\text{NO}_3)_2$  and  $75 \mu\text{M NaI}$ , and (c) microplates formed with  $\text{CuCl}_2$  and  $75 \mu\text{M NaI}$ . (d–f) Tafel plots for two Cu single-crystal electrodes obtained with the same solutions as for (a)–(c), respectively. The original LSVs are shown in Figure S5. The concentrations of Cu precursors, HDA, and AA were 16.4, 49.4, and 50 mM, respectively.

rate of atomic addition to different facets rather than surface energy minimization.<sup>35</sup> If one could directly measure this facet-dependent rate of atomic addition, one could obtain a better understanding of the role shape-directing agents play in controlling anisotropic growth. This understanding could be used to design improved nanostructure syntheses.

We have been using electrochemical measurements on metal single crystals to directly measure the facet-dependent rate of atomic addition in Cu nanowire syntheses.<sup>36–38</sup> For a synthesis in which ethylenediamine was thought to block atomic addition to the {100} facets on the sides of Cu nanowires, electrochemical measurements with single crystals showed that ethylenediamine instead promoted Cu addition to the {111} facets on the ends of Cu nanowires by facilitating the removal of Cu oxide from {111} facets.<sup>36</sup> In another Cu nanowire synthesis, hexadecylamine (HDA) was thought to selectively block atomic addition to the {100} facets on the sides of Cu nanowires while leaving the {111} facets at the ends of nanowires open to atomic addition. However, electrochemical measurements with single crystals showed that HDA passivated both {100} and {111} facets equally. Chloride ions ( $\text{Cl}^-$ ) were required for selectively removing the HDA self-assembled monolayer (SAM) from {111} facets on the nanowire ends but not the {100} facets on nanowire sides.<sup>37</sup> Density functional theory (DFT) calculations showed that facet-selective removal of a HDA SAM from Cu(111) can be obtained with a 0.33 monolayer (ML) coverage of Cl. This last example demonstrates the potential for DFT calculations and single-crystal electrochemistry to provide new molecular-level insights into the facet-selective chemistry that drives the anisotropic growth of nanocrystals.

This study builds upon previous work by using a combination of single-crystal electrochemistry, DFT, and a computational hydrogen electrode approach to explore why the addition of iodide ions ( $\text{I}^-$ ) to HDA-based Cu nanowire synthesis results in the formation of Cu microplates instead of nanowires. Single-crystal electrochemical measurements show that the formation of microplates is due to  $\text{I}^-$  increasing the rate of Cu addition to {100} facets on the sides of microplates while decreasing the rate of Cu addition to the {111} facets on the top and bottom of the microplates. DFT calculations show that  $\text{I}^-$  has a stronger binding affinity for Cu than  $\text{Cl}^-$  and that it replaces  $\text{Cl}^-$  and HDA on both Cu(100) and Cu(111), even when the solution-phase concentration of  $\text{I}^-$  is 100 times lower than  $\text{Cl}^-$ . While Cu nanowire formation is predicted (and observed) in solutions containing chloride and HDA, a strong thermodynamic driving force occurs for microplate growth when a small amount of iodide is added to the chloride–HDA solution, consistent with the experiment. This study thus adds the first clear example to the literature of anisotropic nanostructure growth in the presence of a shape-directing agent that is adsorbed isotropically.

## RESULTS AND DISCUSSION

**Experimental Effects of Halides on Cu Nanostructure Growth.** The synthetic results shown in Figure 1a–c demonstrate the dramatic effect of halide ions on Cu nanocrystal growth. The addition of  $\text{Cl}^-$  to a growth solution containing a Cu(II) precursor, HDA, and ascorbic acid (AA) (herein referred to as a HDA– $\text{Cl}^-$  solution) results in pentagonally twinned Cu nanowires (Figure 1a). We have previously shown that nanowire growth is due to the selective removal of a HDA SAM on the {111} facets at the ends of the

nanowire, while the  $\{100\}$  facets on the sides of the nanowire remain passivated by a HDA SAM.<sup>37,39–41</sup> If  $\text{Cl}^-$  is not present in the synthesis, or the concentration of  $\text{Cl}^-$  is too low ( $\leq 16.4$  mM), both  $\{111\}$  and  $\{100\}$  facets are passivated by HDA to the same extent, and only Cu nanoparticles form.<sup>37</sup> If  $75 \mu\text{M}$  NaI was added in place of  $\text{Cl}^-$  (forming the HDA– $\text{I}^-$  solution), only nanoparticles were formed (Figure 1b). As we see later, this small amount of  $\text{I}^-$  is not by itself sufficient to remove HDA from the Cu surface. Addition of larger amounts of  $\text{I}^-$  to the synthesis caused the precipitation of CuI (see Figures S1 and S2). As shown in Figure S1a, micron-sized irregular particles were obtained at an  $\text{I}^-$  concentration of 3.28 mM (1/10 of the  $\text{Cl}^-$  concentration used for Cu nanowire growth). When more  $\text{I}^-$  was added, smaller nanoparticles were produced (Figure S1b–d) and the intensities of CuI peaks in the X-ray powder diffraction (XRD) patterns increased. (Figure S2). Microplates were occasionally observed at  $\text{I}^-$  concentrations higher than 9.84 mM but at a low yield, presumably because most of the Cu precursor precipitated as CuI. These results suggest that the combination of HDA and  $\text{I}^-$  is sufficient to induce the formation of Cu microplates, but the precipitation of CuI prevents the formation of a high yield of microplates.

Surprisingly, if  $75 \mu\text{M}$  NaI is added to the HDA– $\text{Cl}^-$  solution (forming the HDA– $\text{Cl}^-$ – $\text{I}^-$  solution), microplates formed instead of nanowires and CuI particles. The presence of  $\text{Cl}^-$  enables  $\text{I}^-$  to induce the formation of microplates at lower concentrations of  $\text{I}^-$  that do not cause precipitation of CuI. The microplates had an average thickness of  $130 \pm 30$  nm, an average width of  $4.0 \pm 1.5 \mu\text{m}$ , and an aspect ratio of 31 (Figures 1c and S3). X-ray diffraction (XRD) patterns further confirmed that all three nanocrystals in Figure 1a–c were metallic Cu (Figure S4).

Selected area electron diffraction patterns acquired with the beam oriented perpendicular to the basal planes of the microplates (see Figure 2a,b) exhibit the  $\{220\}$  reflections characteristic of diffraction along the  $\langle 111 \rangle$  direction and  $1/3\{422\}$  reflections characteristic of diffraction from parallel  $\{111\}$  planar defects.<sup>42–48</sup> These results indicate that the basal surfaces of the microplates consist of  $\{111\}$  facets. These results are consistent with those of many previous studies of platelike structures composed of Ag and Au.<sup>42–48</sup>

Given that transmission electron microscopy (TEM) provides a 2D projection of a three-dimensional (3D) object, it has not yet been proven possible to definitively determine the facets on the sides of platelike crystals grown from fcc metals. However, based on their fcc crystal structure, the fact that the basal planes of microplates consist of two  $\{111\}$  surfaces, and the need to minimize surface energy with low-index planes, most researchers inferred that the sides of nanoplates/microplates consist of 12 alternating  $\{100\}$  and  $\{111\}$  side planes (Table S1).<sup>46,49,50</sup> Models in Figure 2c,d show that the number of twin planes in the structure affects the arrangement of  $\{111\}$  and  $\{100\}$  facets on the sides of microplates. When the number of twin layers is even, the side facets alternate vertically and laterally between  $\{111\}$  and  $\{100\}$  in a checkerboard pattern (Figure 2c). A side view TEM image of a Cu microplate (Figure S6) exhibits the structure of this model. The angles between the basal plane and two side facets are  $110$  and  $125^\circ$ , corresponding to the theoretical angles between  $(111)$  and  $(\bar{1} \ 11)$  (i.e.,  $109.5^\circ$ ) and between  $(111)$  and  $(\bar{1}00)$ , respectively. When the number of twin layers is odd, the  $\{111\}$  and  $\{100\}$  facets alternate laterally in

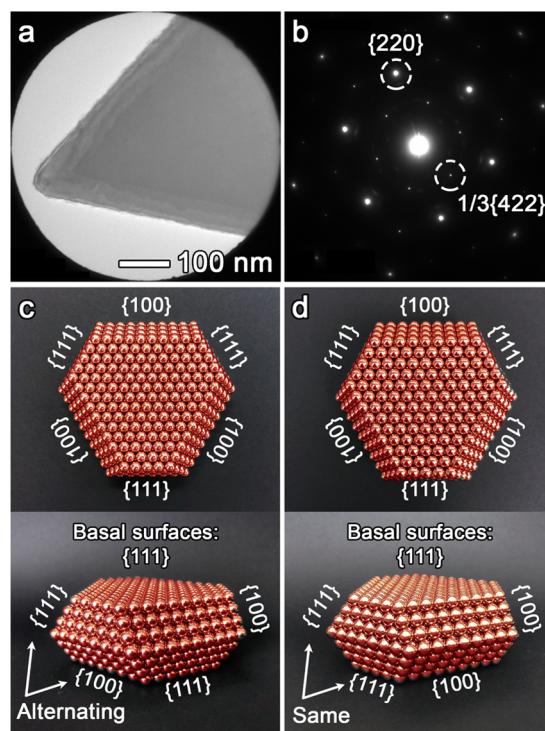


**Figure 2.** (a) Transmission electron microscopy (TEM) image of a part of a Cu microplate and (b) the corresponding electron diffraction pattern. Two models demonstrating the atomic arrangement of Cu in hexagonal plates using a face-centered cubic packing of spherical magnets (c) with an even number of twin defects and (d) an odd number of twin defects. Note that real microplates also likely contain a number of  $\{111\}$  stacking faults.<sup>46,48</sup>

columns (Figure 2d). We note that this simplified model does not reflect evidence from TEM images showing that multiple planar defects can be evenly or asymmetrically distributed across a particle,<sup>20,42,44,48,51</sup> but such structures also have a mixture of  $\{111\}$  and  $\{100\}$  facets on their sides. Based on these structures, the change in the growth mode from nanowires to microplates with the addition of  $\text{I}^-$  implies that an inversion in facet activity occurs such that greater Cu addition takes place on  $\{100\}$  than  $\{111\}$ .

It should be noted that nanowires grow from 5-fold twinned decahedra, while microplates grow from nuclei with parallel twin planes. In addition to influencing the rate of atomic addition to  $\{111\}$  and  $\{100\}$  facets, the addition of iodide ions may influence nucleation such that a greater proportion of seeds has parallel twin planes. We have attempted to investigate the nucleation of Cu seed crystals in alkylamine-halide syntheses by taking samples at multiple time points. The earliest time point at which copper nanocrystals could be found in the HDA– $\text{Cl}^-$ – $\text{I}^-$  solution was at 30 min. These particles were washed with acetonitrile (to remove the white CuCl precipitate), isopropyl alcohol (IPA), hexane (to remove HDA), and 50/50 vol % IPA/water. Even after these washing steps, residual organic residue made it difficult to obtain clear images of the nanocrystals, and the nanocrystals were already over 200 nm in diameter (Figure S7). A modified washing procedure with dimethyl sulfoxide (DMSO) was developed to remove residual organic material, but the washing procedure dissolved small seeds, so that the earliest time point at which nanocrystals could be isolated was 40 min in the HDA– $\text{Cl}^-$ – $\text{I}^-$  solution and 60 min in the HDA– $\text{Cl}^-$  solution (see Figure

S8). Thus, due to the presence of CuCl precipitate and HDA, it proved impossible for us to isolate small ( $\sim 20$  nm) nanoparticle seeds and study the impact of iodide on the crystal structure of seeds. We note that there is no previous study of Cu seeds in the alkylamine synthesis. Nevertheless, given the clear difference in the morphology of the nanocrystals at the earliest time points in the reaction (see Figure S8), we expect that the presence of iodide increased the number of seeds with parallel planar defects.

However, a change in the crystal structures of the seeds cannot by itself be responsible for the formation of Cu microplates. Anisotropic growth is also necessary. For example, if we assume that the microplate seeds start with similar dimensions as silver microplate seeds (e.g., 45 nm wide, 5 nm thick), they will have an aspect ratio of 9.<sup>52</sup> If they then grow isotropically to the scale of  $\sim 1$   $\mu\text{m}$ , they will have an aspect ratio of 1.04 (1.045  $\mu\text{m}$  wide, 1.005  $\mu\text{m}$  thick). This is illustrated in Figure S9. In contrast, Cu microplates have an aspect ratio of 31. This example illustrates that facet-dependent atomic addition of Cu is necessary for the anisotropic growth of the Cu microplates.

Further evidence for the role of halides in facet-selective growth can be obtained from using nanowires and microplates as seeds in the HDA-Cl<sup>-</sup>I<sup>-</sup> and HDA-Cl<sup>-</sup> solutions, respectively. If the HDA-Cl<sup>-</sup>I<sup>-</sup> solution promotes atomic addition to {100} facets, Cu nanowire seeds should grow laterally in this solution because their side facets are {100}. Figure S10 shows that the diameter of the nanowires increased by 3.4 times (before seeded growth: 170  $\pm$  70 nm, after: 580  $\pm$  110 nm). This result is consistent with the hypothesis that the adsorption of I<sup>-</sup> on the surface of a Cu nanostructure results in preferential atomic addition to {100} facets. Second, the HDA-Cl<sup>-</sup> solution should result in passivation of {100} facets on the sides of the microplate, resulting in preferential atomic addition to the {111} facets on the top and bottom of the microplates. Figure S11 shows that the thickness of the microplates increased by 2.3 times while their widths did not significantly change (before seeded growth: 4.0  $\pm$  1.5  $\mu\text{m}$ , after: 4.4  $\pm$  1.0  $\mu\text{m}$ ) in the HDA-Cl<sup>-</sup> solution. This result indicates that a HDA-Cl<sup>-</sup> solution normally used to grow Cu nanowires promoted the atomic addition of Cu onto {111} facets while passivating {100} facets. The result is also consistent with the hypothesis that the sides of the Cu microplates in part consist of {100} facets.

**Effect of Halides on Single-Crystal Electrochemical Measurements.** To test the hypothesis that I<sup>-</sup> inverts the facet activity, electrochemical measurements with Cu(111) and Cu(100) single-crystal electrodes were performed in the same solutions used to grow the nanocrystals.<sup>36–38</sup> In the synthesis solution, Cu-alkylamine complexes are reduced by ascorbic acid. As described by the mixed potential theory,<sup>53,54</sup> the spontaneous overall reaction occurs at a mixed potential ( $E_{\text{mp}}$ ) at which the two half-reactions (Cu ion reduction and ascorbic acid oxidation) have equal rates. As all of the electrons produced by oxidation are consumed by reduction, the net current at the mixed potential is zero. The current for either half-reaction at the mixed potential gives the reaction rate for Cu nanocrystal growth. For reactions that are charge transfer-limited, the magnitude of the half-reaction current at  $E_{\text{mp}}$  (referred to as  $j_{\text{mp}}$ ) can be obtained from a Tafel plot of a linear sweep voltammogram in the reaction solution.

In the HDA-Cl<sup>-</sup> solution (Figure 1d),  $j_{\text{mp}}^{(111)}$  was 12.7 times greater than  $j_{\text{mp}}^{(100)}$  (see also Table 1). In contrast, Table 1

**Table 1. Current Density at the Mixed Potential ( $j_{\text{mp}}$ ) for Two Single-Crystal Electrodes with Different Additives<sup>a</sup>**

shape	additives	$j_{\text{mp}}^{(100)}$	$j_{\text{mp}}^{(111)}$	$j_{\text{mp}}^{(100)}/j_{\text{mp}}^{(111)}$	ref
particles	HDA	11.09	11.71	0.95	37
	HDA-I <sup>-</sup>	10.96	11.59	0.95	Figure 1e
nanowires	HDA-Cl <sup>-</sup>	12.11	153.78	0.079	Figure 1d
microplates	HDA-Cl <sup>-</sup> I <sup>-</sup>	48.64	18.71	2.60	Figure 1f

<sup>a</sup>The concentrations of Cu ions, HDA, Cl<sup>-</sup>, I<sup>-</sup>, and AA were 16.4, 49.4, 32.8, 0.075, and 50 mM, respectively.

shows that  $j_{\text{mp}}$  for Cu(111) and Cu(100) are the same if Cl<sup>-</sup> is not present. This result shows that the presence of Cl<sup>-</sup> activates Cu(111) but not Cu(100), thus explaining why pentagonally twinned Cu nanowires with {111} facets on their ends and {100} facets on their sides only grow when Cl<sup>-</sup> is present in the reaction solution.<sup>37</sup> The  $j_{\text{mp}}$  values in the HDA-I<sup>-</sup> solution (Figure 1e) were similar to those of the case when the solution contains Cu-HDA complexes and AA without any halide ions (Table 1).<sup>37</sup> The agreement between the two measurements indicates that with 75  $\mu\text{M}$  I<sup>-</sup>, both (111) and (100) electrodes were passivated by HDA without any facet-selective behavior ( $j_{\text{mp}}^{(100)}/j_{\text{mp}}^{(111)} = 0.95$ ). This result means that the low I<sup>-</sup> concentration (i.e., 660 and 440 times lower than HDA and Cl<sup>-</sup>, respectively) cannot disrupt the HDA SAM on either facet.

However, the addition of I<sup>-</sup> to the HDA-Cl<sup>-</sup> solution (i.e., HDA-Cl<sup>-</sup>I<sup>-</sup> solution) changed the facet-selective activity. Figure 1f and Table 1 show that the  $j_{\text{mp}}$  for the (100) electrode is 2.60 times greater than for the (111) electrode, the opposite of what was observed in the HDA-Cl<sup>-</sup> solution (Figure 1d). This inversion is consistent with the hypothesis that I<sup>-</sup> facilitates greater Cu atomic addition to the {100} edge facets than to the {111} basal planes, ultimately resulting in microplate formation. The electrochemical measurements shown in Figure 1e,f also indicate that the presence Cl<sup>-</sup> facilitates I<sup>-</sup> adsorption on Cu surfaces. For the case of Cu(111), Cl<sup>-</sup> facilitates I<sup>-</sup> adsorption by completely detaching HDA from the surface. For Cu(100), coadsorption of Cl<sup>-</sup> with HDA weakens the HDA-Cu bond and creates a different surface phase that may lower the kinetic barrier to I<sup>-</sup> adsorption.<sup>37,40</sup>

**Effect of Iodide Concentration.** Additional evidence for the role of I<sup>-</sup> was obtained by measuring the  $j_{\text{mp}}^{(111)}$  and  $j_{\text{mp}}^{(100)}$  values of the HDA-Cl<sup>-</sup>I<sup>-</sup> solution at various I<sup>-</sup> concentrations (Figure 3a). Increasing the I<sup>-</sup> concentration decreased  $j_{\text{mp}}^{(111)}$  while increasing  $j_{\text{mp}}^{(100)}$ . Figure 3b shows this increase in the  $j_{\text{mp}}^{(100)}/j_{\text{mp}}^{(111)}$  ratio was accompanied by an increase in the aspect ratio of microplates. Figure S12 indicates that increasing I<sup>-</sup> concentration resulted in a decrease in microplate thickness and an increase in microplate width. Also, when the value of  $j_{\text{mp}}^{(100)}/j_{\text{mp}}^{(111)}$  was over 2.5, the percent of microplates exceeded 85%, whereas the yield decreased to 36% when the  $j_{\text{mp}}^{(100)}/j_{\text{mp}}^{(111)}$  was 0.31 (see Figure S13). These results indicate that  $j_{\text{mp}}^{(100)}/j_{\text{mp}}^{(111)}$  can be used as a predictor for the formation of microplates and that the effects of I<sup>-</sup> on the facet-selective activity of the single-crystal electrodes are likely similar to the mechanisms by which I<sup>-</sup> causes anisotropic growth of microplates.

**Hypothesis for the Role of Iodide.** The schematic in Figure 4 illustrates our hypothesis for how I<sup>-</sup> activates {100} facets while passivating {111} facets. In the absence of I<sup>-</sup> (left

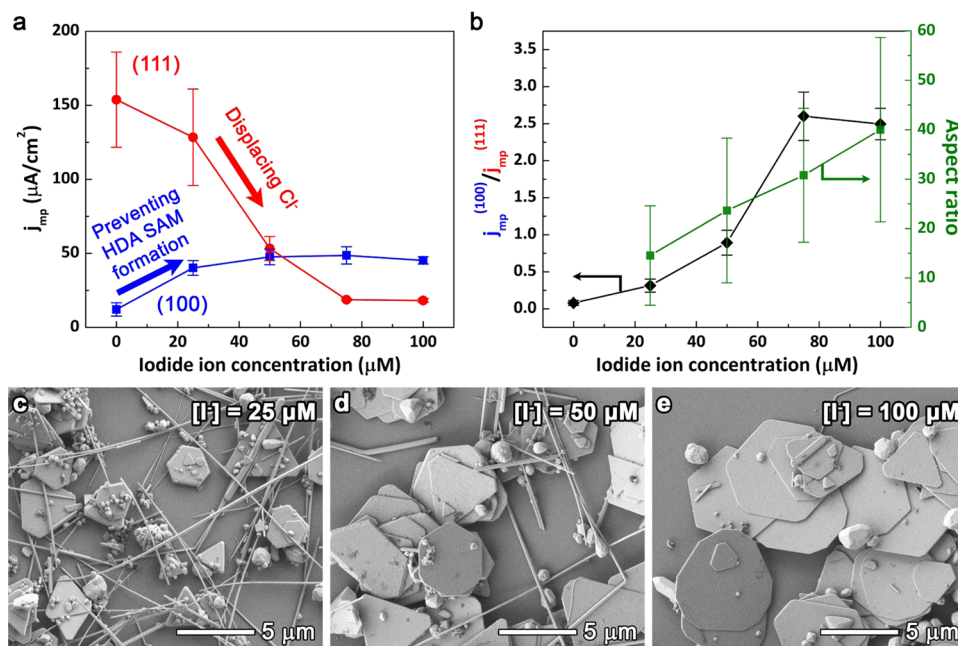


**Figure 3.** (a) Values of  $j_{mp}^{(100)}$  and  $j_{mp}^{(111)}$  vs  $I^-$  concentration. (b) Values of  $j_{mp}^{(100)}/j_{mp}^{(111)}$  (diamonds) and the aspect ratio of microplates (squares) vs  $I^-$  concentration. The original Tafel plots are shown in Figure S14. Representative scanning electron microscope (SEM) images at  $I^-$  concentrations of (c) 25  $\mu M$ , (d) 50  $\mu M$ , and (e) 100  $\mu M$ . The synthetic results with 0 and 75  $\mu M$   $I^-$  are shown in Figure 1a,c.

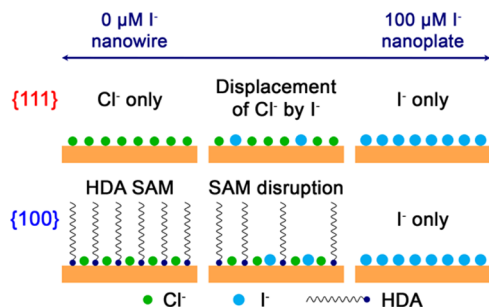


**Figure 4.** Schematic diagram of Cu {111} and {100} facets in a HDA–Cl<sup>-</sup> solution with different concentrations of  $I^-$ .

side of the schematic), the {111} surface is covered exclusively by Cl<sup>-</sup> (which activates the surface for atomic addition) and the {100} surface is passivated by a HDA SAM with a 1/3 ML of co-adsorbed Cl<sup>-</sup>.<sup>37</sup> Addition of  $I^-$  replaces Cl<sup>-</sup> on the {111} facet, leading to its passivation. The Cl<sup>-</sup> adsorbed on a Cu surface has been shown to activate Cu deposition,<sup>55</sup> but adsorbed  $I^-$  suppresses Cu deposition.<sup>56</sup> The relatively covalent Cu–I bond is stronger than the relatively ionic Cu–Cl bond and involves a greater amount of charge transfer from  $I^-$  to Cu. This stronger interaction between  $I^-$  and Cu hinders atomic addition.<sup>57,58</sup>

An alternative explanation is that {111} basal facets are passivated by HDA in the HDA–Cl<sup>-</sup>– $I^-$  solution. To test this alternative hypothesis, we compared the linear sweep voltammetry (LSV) with a Cu(100) electrode in a HDA–Cl<sup>-</sup> solution to the LSV with a Cu(111) electrode in a HDA–Cl<sup>-</sup>– $I^-$  solution (Figure S15). The LSV of a Cu(100) electrode in a HDA–Cl<sup>-</sup> solution has a current plateau between –0.04 and 0.05 V, indicating that Cu reduction is inhibited by a passivating HDA SAM.<sup>37</sup> However, no current plateau was observed for the Cu(111) electrode in the HDA–Cl<sup>-</sup>– $I^-$  solution, suggesting that no HDA SAM was present on the (111) surface. These results indicate that the inhibition of

Cu atomic addition on the {111} basal planes was caused by adsorbed  $I^-$ .

As illustrated in the bottom of Figure 4,  $I^-$  disrupts the HDA SAM on the {100} facet, resulting in a surface covered by  $I^-$ . Since the HDA SAM is a better inhibitor of Cu reduction than adsorbed  $I^-$  (see Figure S15), the adsorption of  $I^-$  instead of the HDA SAM led to an increase in the  $j_{mp}^{(100)}$  (Figure 3a). When the concentration of  $I^-$  exceeded 75  $\mu M$  (Figure 3a), there were no significant changes in the  $j_{mp}$  for either single-crystal electrode, implying that each electrode surface was saturated with  $I^-$ . This result suggests that the growth of microplates occurs when both {111} basal and {100} edge surfaces of microplates are covered by adsorbed  $I^-$  alone.

**Theoretical Calculations.** Electrochemical measurements using single-crystal electrodes suggest that  $I^-$  disrupted HDA SAMs on {100} facets and replaced Cl<sup>-</sup> on {111} facets. It was also observed that the growth of Cu microplates occurred due to a 2.60 times greater rate of Cu deposition on {100} facets than {111} facets (Figure 1f) even though both facets were covered by  $I^-$ . These experimental observations elicit two questions. First, is the replacement of HDA and Cl<sup>-</sup> adlayers by  $I^-$  thermodynamically favorable? Second, how can the presence of  $I^-$  on both facets cause anisotropic growth of Cu microplates?

To answer these questions, we used ab initio thermodynamics based on dispersion-corrected DFT and the computational hydrogen electrode method.<sup>59</sup> All calculations were performed using the Vienna Ab initio simulation package (VASP).<sup>60–62</sup> Details of the DFT calculations can be found in the Methods Section, as well as in the Supporting Information. As we discuss below, these calculations establish that, under the experimental conditions, there is a thermodynamic driving force for the replacement of HDA and Cl<sup>-</sup> adlayers by  $I^-$  and for the growth of microplates when  $I^-$  is adsorbed on both facets.

**Calculated Effect of Halides on HDA Monolayer Desorption.** To understand the influence of  $I^-$  on HDA adsorption, we studied the coadsorption of HDA and I as a function of I coverage on two Cu surfaces. The lowest I coverage studied was 0.25 ML with a HDA coverage of 0.25 ML. At this coverage, HDA was chemisorbed on Cu(100) (Figure S16a). In contrast, HDA was physically adsorbed on Cu(111) at the same coverage (Figure S16b). As the I coverage increased to 0.33 ML, HDA formed a physically adsorbed layer above the Cu(100)–I interface (Figure 5a). On

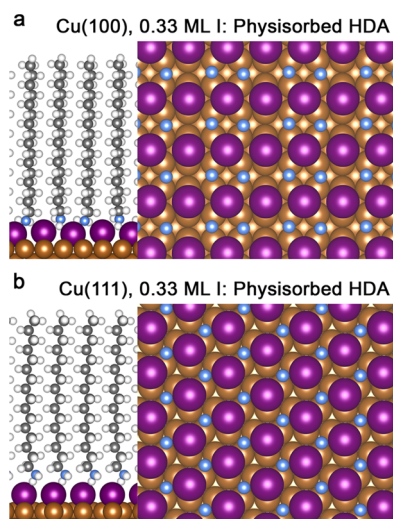


**Figure 5.** Side and top (showing N and I atoms only) views for optimized binding configurations of Cu–I–HDA systems at 0.33 ML I coverage on (a) Cu(100) and (b) Cu(111) (brown: Cu, purple: I, blue: physisorbed N, gray: C, and white: H).

Cu(111), the HDA adlayer remained weakly bound to the substrate by vdW attraction at the higher I coverage of 0.33 ML (Figure 5b). A higher I coverage of 0.50 ML on Cu(100) also led to physisorbed HDA.

Table S2 shows that the binding of HDA to both Cu surfaces grew progressively weaker as the coverage of I increased.<sup>37</sup> It was also confirmed that the effect of  $I^-$  on a HDA SAM was greater than that of Cl (Table 2). At 0.33 ML

**Table 2.** HDA Adsorption at Various Halogen Surface Coverages (P: Physisorbed HDA, C: Chemisorbed HDA)

halogen	Cu facets	halogen surface coverage (ML)			
		0.25	0.33 <sup>a</sup>	0.4	0.5
I	(111)	P	P	P	P
	(100)	C	P	P	P
Cl <sup>bF</sup>	(111)	C	P	P	P
	(100)	C	C	mixed <sup>c</sup>	P

<sup>a</sup>Surface coverages of I and Cl for microplates and nanowires, respectively. <sup>bF</sup>rom ref 37. <sup>c</sup>Physisorbed + chemisorbed.

coverage of I or Cl, HDA SAMs were removed from both (100) and (111) by adsorbed I, whereas Cl replaced the HDA SAM on (111) but not on (100). A Cl coverage of 0.5 ML was necessary to remove chemisorbed HDA from both (111) and (100) surfaces. The greater effect of I on the disruption of HDA SAMs was due to the larger size of I relative to Cl.

The electrochemical results suggest that the low concentration of  $I^-$  in the microplate growth solution resulted in

adsorption of  $I^-$  on both {111} and {100} facets, with no passivation by HDA on either facet. If the thermodynamically most favorable surface coverage of I is at least 0.25 ML on Cu(111) and 0.33 ML on Cu(100) at the synthetic conditions used in this study, DFT calculations show that both surfaces will either be free from HDA SAMs or contain weakly bound layers, in agreement with the experimental results.

**Calculation of the Preferred Surface Structures of Halogen Monolayers.** We next performed ab initio thermodynamic calculations<sup>63</sup> to determine the preferred surface configurations of adsorbed I, Cl, and HDA under the experimental conditions. The preferred surface configuration was characterized by its surface energy, where the surface energy for a Cu slab containing Cl and/or I and/or HDA ( $\gamma_{Cu-Cl-I-HDA}$ ) is given by eq 1.

$$\gamma_{Cu-Cl-I-HDA} = \frac{(E_{Cu-Cl-I-HDA} - N_{Cu}E_{Cu}^{bulk} - N_{Cl}\mu_{Cl}^{aq} - N_I\mu_{I}^{aq} - N_{HDA}\mu_{HDA}^{aq})}{A_{surf}} - \gamma_{Cu}^{fixed} \quad (1)$$

Here,  $E_{Cu-Cl-I-HDA}$  is the total energy of an optimized Cu surface slab containing Cl, I, and HDA;  $N_{Cu}$  and  $E_{Cu}^{bulk}$  represent the number of Cu atoms in the surface slab and the bulk energy per Cu atom, respectively;  $N_{Cl}$  is the number of adsorbed Cl atoms,  $\mu_{Cl}^{aq}$  is the chemical potential of solution-phase  $Cl^-$ ,  $N_I$  is the number of adsorbed I atoms,  $\mu_{I}^{aq}$  is the chemical potential of aqueous  $I^-$ ,  $N_{HDA}$  is the number of adsorbed HDA molecules,  $\mu_{HDA}^{aq}$  is the chemical potential of solution-phase HDA, and  $A_{surf}$  is the surface area of the slab.  $\gamma_{Cu}^{fixed}$  is the surface energy of a bare Cu surface slab with atoms fixed at the bulk coordinates, which we subtract as a result of performing our calculations with halogen adsorbed on only one side of the slab. We note that the DFT energies in eq 1 can be augmented to consider temperature effects, such as the vibrational entropies of the slab and the bulk. As these effects have been estimated to be negligible in other studies of Cu–halide interfaces,<sup>58</sup> we neglect them here. Additionally, HDA SAMs on the two Cu surfaces in an aqueous environment simulated at 90 °C with molecular dynamics based on our metal–organic many-body force field retain the same structures as those in vacuum DFT calculations,<sup>39,40</sup> indicating that the HDA SAMs in the DFT calculations should reflect those in an aqueous environment at 90 °C. Finally, it should be clear that the chemical potentials in eq 1 are a function of temperature. We return to this point below.

We can use eq 1 to obtain the  $\gamma_{Cu-Cl-I-HDA}$  as a function of  $\mu_{Cl}^{aq}$ ,  $\mu_{I}^{aq}$ , and  $\mu_{HDA}^{aq}$ . The surface with the lowest energy for a given set of chemical potentials is the one predicted to be observed in the experiment. This would create a four-dimensional plot of the  $\gamma_{Cu-Cl-I-HDA}$  as a function of three chemical potentials. To simplify the calculations, we note that the experiments are run at a constant concentration (i.e., chemical potential) of HDA. We know that the synthetic conditions for Cu microplates were exactly the same as those for Cu nanowires except that a small amount of  $I^-$  was introduced (75–100  $\mu$ M). We can thus estimate  $\mu_{HDA}^{aq}$  in the synthesis of microplates from the conditions used to produce Cu nanowires,<sup>37</sup> considering only Cu,  $Cl^-$ , and HDA. Specifically, we know that nanowires grow when Cu(100) contains both adsorbed  $Cl^-$  and a chemically adsorbed HDA SAM, but Cu(111) contains only adsorbed  $Cl^-$  with physically adsorbed HDA.<sup>37</sup> From ab initio thermodynamics results for the Cu–Cl–HDA system (details are in ref 64), we

determined a range of values for  $\mu_{\text{HDA}}^{\text{aq}}$ , which resulted in HDA and Cl adsorbed on Cu(100) but only Cl on Cu(111). To further clarify the  $\mu_{\text{HDA}}^{\text{aq}}$  and likely surface environments in the experiments, we selected values for three  $\mu_{\text{HDA}}^{\text{aq}}$  that could theoretically result in nanowires due to the chemisorption of HDA on Cu(100) but not on Cu(111).<sup>64</sup>

For each fixed value of the  $\mu_{\text{HDA}}^{\text{aq}}$ , we identify the surface configurations with the minimum surface energies as a function of  $\mu_{\text{Cl}^-}$  and  $\mu_{\text{I}^-}$ . To create the phase diagram, we create surfaces with Cl, HDA, and I in various proportions. In total, 38 different surface structures, 16 on Cu(100) and 22 on Cu(111), were studied. These structures include those listed in Table 2, as well as those in Tables S3 and S4 in the Supporting Information. Though we considered 22 possible structures with co-adsorbed Cl and I (see Table S3), none of these turned out to be significant.

Figure 6 shows phase diagrams of the lowest energy surfaces as a function of  $\mu_{\text{Cl}^-}$  and  $\mu_{\text{I}^-}$  for Cu(111) (Figure 6a) and

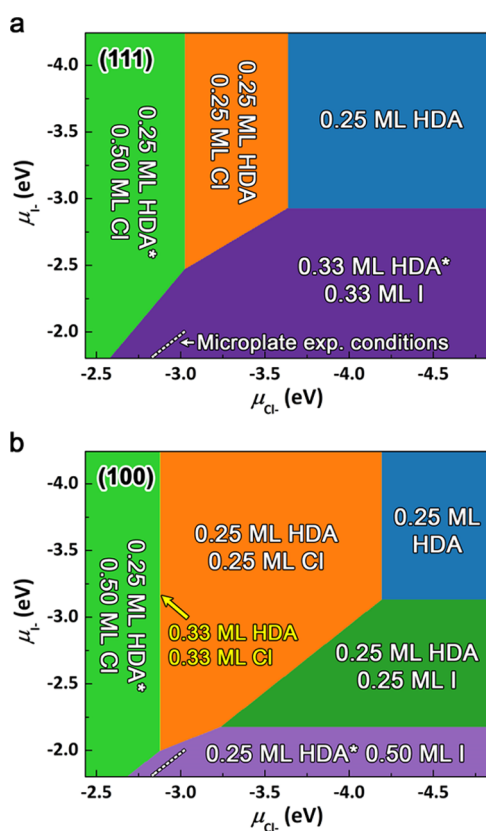


**Figure 6.** Equilibrium surface structures on (a) Cu(111) and (b) Cu(100) as a function of  $\mu_{\text{Cl}^-}$  and  $\mu_{\text{I}^-}$  for fixed  $\mu_{\text{HDA}}^{\text{aq}}$ . The dashed lines represent the range of possible chemical potentials that correspond to the experimental conditions of 49.4 mM HDA, 32.8 mM  $\text{Cl}^-$ , and 100  $\mu\text{M}$   $\text{I}^-$ . HDA coverages marked by \* indicate physisorbed HDA. CuCl forms at  $\mu_{\text{Cl}^-}^{\text{aq}} > -2.43$  eV and CuI forms at  $\mu_{\text{I}^-}^{\text{aq}} > -1.80$  eV.

Cu(100) (Figure 6b) at an intermediate value of  $\mu_{\text{HDA}}^{\text{aq}}$ . Phase diagrams with low and high values of  $\mu_{\text{HDA}}^{\text{aq}}$  (which bracket the feasible range of HDA chemical potentials) are shown in Figures S17 and S18, respectively. Various regions of HDA, I, and Cl coverages are labeled. The  $x$  and  $y$  axes in Figure 6 represent the  $\text{Cl}^-$  and  $\text{I}^-$  chemical potentials, respectively, at which solid CuCl and CuI are predicted to form, i.e., CuCl forms at  $\mu_{\text{Cl}^-}^{\text{aq}} > -2.43$  eV and CuI forms at  $\mu_{\text{I}^-}^{\text{aq}} > -1.80$  eV.

To relate the results in Figure 6 to the experimental results, we need to have explicit expressions for the  $\mu_{\text{Cl}^-}^{\text{aq}}$  and  $\mu_{\text{I}^-}^{\text{aq}}$ . For this, we used the computational hydrogen electrode method, following its adaptation by Gossenberger and co-workers.<sup>59,65</sup> In this method, the electrochemical potential for a halide  $\text{X}^-$  in solution can be obtained for the redox reaction ( $1/2\text{X}_2 + \text{e}^- \leftrightarrow \text{X}^-$ ) using

$$\mu_{\text{X}^-}^{\text{aq}} - \mu_{\text{e}^-} = \frac{1}{2}E_{\text{X}_2}^{\text{DFT}} + e(U_{\text{SHE}} - U_{\text{X}_2}) + k_{\text{B}}T \ln a_{\text{X}^-} \quad (2)$$

where  $E_{\text{X}_2}^{\text{DFT}}$  is the DFT energy of a diatomic  $\text{X}_2$  molecule in the gas phase,  $U_{\text{SHE}}$  is the electrode potential using the standard hydrogen electrode as the reference,  $U_{\text{X}_2}$  is the standard reduction electrode potential for  $\text{X}_2$  (the calibrated values of +1.28 V for  $1/2 \text{Cl}_2$  and +0.53 V for  $1/2 \text{I}_2$  are used based on the experimental temperature of 90 °C, as suggested by Bratsch<sup>66</sup>), and the last term accounts for deviations of the solution from standard conditions using the activity  $a_{\text{X}^-}$ .<sup>67</sup> Using eq 2, the difference between  $\mu_{\text{I}^-}^{\text{aq}}$  and  $\mu_{\text{Cl}^-}^{\text{aq}}$  in the syntheses of microplates can be written as eq 3.

$$\mu_{\text{I}^-}^{\text{aq}} = \mu_{\text{Cl}^-}^{\text{aq}} + \frac{1}{2}(E_{\text{I}_2}^{\text{DFT}} - E_{\text{Cl}_2}^{\text{DFT}}) + e(U_{\text{Cl}_2} - U_{\text{I}_2}) + k_{\text{B}}T \ln \left( \frac{a_{\text{I}^-}}{a_{\text{Cl}^-}} \right) \quad (3)$$

Since the concentrations of  $\text{Cl}^-$  and  $\text{I}^-$  were low in the syntheses, we simplified eq 3 by taking the activities as the concentrations, based on the assumption of an ideal solution. Then, the unknowns in eq 3 are the chemical potentials. We can estimate  $\mu_{\text{Cl}^-}^{\text{aq}}$  in the synthesis of microplates from the  $\mu_{\text{Cl}^-}^{\text{aq}}$  in the Cu nanowire synthesis since the synthetic conditions for Cu microplates were exactly the same as those for Cu nanowires except for the small amount of  $\text{I}^-$ . From ab initio thermodynamics results for the Cu–Cl–HDA system (also see the discussion in the Supporting Information and Table S4), we found that a  $\mu_{\text{Cl}^-}^{\text{aq}}$  value ranging from  $-3.022$  to  $-2.738$  eV could lead to the growth of nanowires.<sup>64</sup> The corresponding range of  $\mu_{\text{I}^-}^{\text{aq}}$  was then determined to be  $-1.998$  to  $-1.714$  eV using eq 3 with the experimental  $\text{I}^-$  concentration of 100  $\mu\text{M}$ .

The short dashed lines in Figure 6 correspond to the range of  $\mu_{\text{Cl}^-}^{\text{aq}}$  and  $\mu_{\text{I}^-}^{\text{aq}}$  values that match the experimental range for microplate formation. Under the experimental conditions, we predict that Cu(111) is covered with 0.33 ML I, while Cu(100) is covered with 0.5 ML I. Note that HDA is physisorbed rather than chemisorbed to both surfaces, consistent with experimental results. Decreasing the  $\text{I}^-$  concentration from 100  $\mu\text{M}$  shifts the short dashed line in Figure 6 vertically to lower values of  $\mu_{\text{I}^-}^{\text{aq}}$ . Thus, the system shifts to a region in which Cu(111) contains 0.5 ML of Cl (Figure 6a). Figure 6b shows that Cu(100) could exist in three possible regions at lower values of  $\mu_{\text{I}^-}^{\text{aq}}$ : (1) 0.25 ML of co-chemisorbed Cl and HDA, (2) 0.33 ML of co-chemisorbed Cl and HDA, or (3) 0.5 ML of Cl with physisorbed HDA. Nanowire formation could occur in regions (1) and (2). This is consistent with the experimental observations in Figure 3.

It is of interest to ascertain how varying  $\mu_{\text{HDA}}^{\text{aq}}$  changes the results in Figure 6. As discussed in the Supporting Information (Figures S17 and S18), increasing or decreasing  $\mu_{\text{HDA}}^{\text{aq}}$  within a range consistent with experimental observations for nanowire

formation could also lead to microplate formation in the experimental concentration range for iodide.

Figure 7 shows the ratio of the surface energies of Cu(111) to Cu(100) ( $\gamma^{111}/\gamma^{100}$ ) for all of the conditions in Figure 6 as a

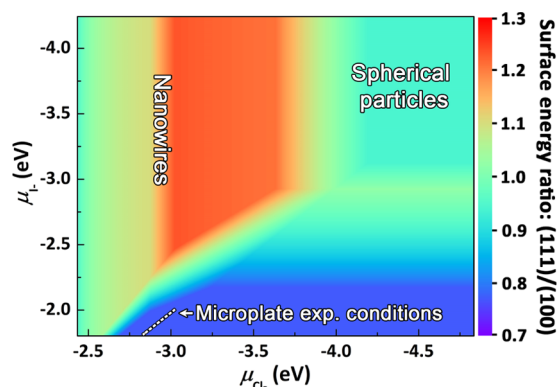


**Figure 7.** Ratio of the surface energies of Cu(111) to Cu(100) obtained from eq 1 for the conditions in Figure 6 as a function of  $\mu_{\text{Cl}}^{\text{aq}}$  and  $\mu_{\text{I}}^{\text{aq}}$ . The labeled regions are where nanowires, spherical particles, and microplates are observed experimentally. The dashed line represents the range of possible chemical potentials that corresponds to the experimental conditions of 49.4 mM HDA, 32.8 mM  $\text{Cl}^-$ , and 100  $\mu\text{M}$   $\text{I}^-$ .

function of  $\mu_{\text{Cl}}^{\text{aq}}$  and  $\mu_{\text{I}}^{\text{aq}}$ . Here, we see that when  $\mu_{\text{I}}^{\text{aq}}$  is sufficiently low, there is a region (in orange–red) for which  $\gamma^{100} < \gamma^{111}$ . This is the region where there is a thermodynamic driving force for the formation of structures bounded by {100} facets (i.e., nanowires). There is an additional kinetic advantage for {100}-faceted structures in a narrow region where Cu(100) contains co-chemisorbed HDA and  $\text{Cl}^-$ , while Cu(111) contains  $\text{Cl}^-$  with physisorbed HDA.<sup>64</sup> At the experimental conditions for microplate formation (indicated by the dashed line),  $\gamma^{111}$  is 1.4 times lower than  $\gamma^{100}$ , providing a driving force for {111} facet formation and microplate growth. This thermodynamic driving force helps to explain why the rate of atomic addition to Cu(100) is 2.5 times faster than that to Cu(111) (Figure 3b). Additionally, adsorbed  $\text{I}^-$  might affect Cu surface diffusion, so that the {100} microplate sides become a sink for diffusing Cu atoms. A similar mechanism was recently proposed for the growth of Ag nanowires.<sup>68</sup> This role of surface diffusion may also explain why the aspect ratio of the microplates ( $\cong 31$ ) is larger than the  $j_{\text{mp}}^{(100)}/j_{\text{mp}}^{(111)}$  ratio of the Cu single-crystal electrodes ( $j_{\text{mp}}^{(100)}/j_{\text{mp}}^{(111)} = 2.6$ ).

When  $\mu_{\text{Cl}}^{\text{aq}}$  and  $\mu_{\text{I}}^{\text{aq}}$  are both low, both surfaces are covered by HDA and  $\gamma^{111}/\gamma^{100} \approx 1$ . In this region of concentrations/chemical potentials (upper right corner of Figure 7), there is no strong driving force for either surface, consistent with the formation of spherical particles in the absence of  $\text{Cl}^-$  and  $\text{I}^-$  in solution.<sup>37</sup> For reference, the computed surface energy ratio for the bare Cu surfaces is  $\gamma^{111}/\gamma^{100} \approx 0.91$ , which indicates that HDA and  $\text{Cl}^-$  adsorption lowers  $\gamma^{100}$  more than  $\gamma^{111}$ , while  $\text{I}^-$  adsorption lowers  $\gamma^{111}$  more than  $\gamma^{100}$ . We note that Figure 7 could be used to predict Wulff shapes for single-crystal equilibrium structures. In the present study, however, we have kinetic structures and Figure 7 illustrates the thermodynamic driving forces for these structures.

## CONCLUSIONS

The combination of synthetic results, single-crystal electrochemistry, and theoretical calculations presented herein demonstrates that it is possible for anisotropic growth of nanostructures to occur even when the shape-directing agent, in this case  $\text{I}^-$ , adsorbs isotropically. This is in contrast to the case of Cu nanowire growth, which is mediated by the presence of a HDA SAM on the nanowire sides and the absence of HDA on the nanowire ends (due to displacement by  $\text{Cl}^-$ ).<sup>37</sup> The presence of HDA on only the sides of nanowires bears resemblance to the original capping-agent hypothesis, in which an organic additive selectively blocks atomic addition to certain facets to cause anisotropic growth. However, in the case of microplates, ab initio thermodynamics calculations indicate that both the edges and basal planes of Cu microplates were covered by chemisorbed  $\text{I}^-$  and physisorbed HDA under the experimental conditions. Single-crystal electrochemical experiments further show that  $\text{I}^-$  is adsorbed to both {111} and {100} facets. The isotropic chemisorption of  $\text{I}^-$  lowered the surface energy of the {111} facets on the basal planes relative to the {100} facets on the edges of the microplates, creating a thermodynamic driving force for microplate growth.

## METHODS SECTION

**Synthesis of Cu Nanocrystals.** Cu nanowires were synthesized by preparing 15 mL of an aqueous solution containing 16.4 mM  $\text{CuCl}_2 \cdot 2\text{H}_2\text{O}$  ( $\geq 99.0\%$ , Sigma-Aldrich) and 49.4 mM hexadecylamine (HDA, 90%, Aldrich) in a 20 mL glass vial and stirring rapidly for 24 h. Ascorbic acid (50 mM,  $\geq 99\%$ , Sigma-Aldrich) was added to the reaction solution, which was then vortexed for 30 s and placed in a 90 °C oven for 17 h to grow Cu nanowires. Cu microplates were synthesized by adding the appropriate concentration of NaI ( $\geq 99.5\%$ , Sigma-Aldrich) to the  $\text{CuCl}_2$ -HDA solution above and then following the nanowire synthesis procedure. Cu nanoparticles were synthesized by replacing  $\text{CuCl}_2$  in the microplate synthesis with 16.4 mM  $\text{Cu}(\text{NO}_3)_2 \cdot 2.5\text{H}_2\text{O}$  (98%, Sigma-Aldrich). In this article, the reaction solutions for nanowires and microplates are referred to as HDA- $\text{Cl}^-$  and HDA- $\text{Cl}^-$ - $\text{I}^-$  solutions, respectively. The procedures for seed-mediated synthesis are described in the Supporting Information.

All of the products were purified by first centrifuging the reaction solution for 10 min at 1500 rpm and discarding the supernatant. The isolated Cu nanocrystals were then washed sequentially with isopropyl alcohol (IPA), hexane, and a solution containing 40% IPA and 60% deionized water by volume. The suspensions were centrifuged at 1500 rpm for 10 min between each wash. Images of the Cu nanocrystals were taken with a scanning electron microscope (SEM, Apreo S, Thermo Fisher Scientific, and FEI XL30, SEM-FEG) in the Shared Materials Instrumentation Facility at Duke University. Scanning transmission electron microscopy (STEM) and selected area electron diffraction were performed with the ThermoFisher Titan 80–300 scanning transmission electron microscope in the Analytical Instrumentation Facility at NC State University. The samples for imaging were prepared by resuspending the purified products in IPA and drop-casting onto silicon wafers. X-ray diffraction (XRD, PANalytical X'pert Pro MRD) was performed to check the crystal structures of the products.

**Electrochemical Measurements.** Procedures for electrochemical measurements have been reported in our previous study.<sup>37,38</sup> The electrochemical measurements were performed with the same solutions used for the syntheses of Cu nanocrystals, and the electrolyte temperature was kept at 90 °C using a water bath. A supporting electrolyte (0.2 M  $\text{KNO}_3$ , 99%, Sigma-Aldrich) was additionally added to the solutions to remove any effects of solution resistance on the electrochemical measurements. Electrochemical measurements were performed using a CHI600D potentiostat (CH Instruments, Inc.). A three-electrode system was used in this study,

consisting of Cu single-crystal or polycrystalline electrodes as the working electrode, a Pt wire as the counter electrode, and a Ag/AgCl reference electrode. Before each measurement, the working electrode was mechanically polished with alumina particles (1.0 and 0.3  $\mu\text{m}$ , Buehler) on Nylon pads. The Cu(111) and Cu(100) single-crystal electrodes were subsequently electrochemically polished by applying 1.6 V (vs Pt wire) in phosphoric acid (85%, Acros Organics). Between each polishing step, the electrode was washed with deionized water.

Linear sweep voltammetry (LSV) with the Cu single-crystal electrodes was conducted by sweeping the potential from 0.12 to  $-0.25$  V (vs Ag/AgCl) at a scan rate of 1 mV/s. After adding ascorbic acid to the Cu–HDA-halide solutions, the electrolytes were first heated to 90  $^{\circ}\text{C}$  for 2 min. Then, the single-crystal electrodes were immersed in the electrolyte. After 3 min, the reference and counter electrodes were immersed in the electrolyte, and LSV was started after an additional 2 min. The collected current–potential curves were replotted on the log scale (i.e., Tafel plot) to extract the current density at mixed potential ( $j_{\text{mp}}$ ).<sup>37,38</sup>

**DFT Calculations.** The Vienna Ab initio simulation package (VASP) with the projector augmented-wave method was used for all DFT calculations in this work.<sup>60–62,69,70</sup> The generalized gradient approximation (GGA) with the exchange–correlation functional by Perdew, Burke, and Ernzerhof (PBE) was used.<sup>71</sup> Convergence criteria of  $10^{-6}$  eV for energy and 0.01 eV/Å for forces were used for structural optimizations with an energy cutoff set to 450.00 eV and a Methfessel–Paxton smearing of 0.1 eV. A  $(15 \times 15 \times 1)$   $k$ -point mesh was used for bulk calculations. For optimizations of molecules including  $\text{Cl}_2$ ,  $\text{I}_2$ , and HDA, single-point calculations were applied using a cubic unit cell with a side length of 25.0 Å. A dipole correction was introduced in the surface normal direction within the asymmetric one-side adsorption model. Additional details of the DFT calculations are described in the [Supporting Information](#).

## ■ ASSOCIATED CONTENT

### SI Supporting Information

The Supporting Information is available free of charge at <https://pubs.acs.org/doi/10.1021/acs.chemmater.0c03596>.

Experimental procedures for seed-mediated growth; detailed description of the DFT calculations; additional information for the ab initio thermodynamics study; representative SEM image used to measure the average thickness of Cu microplates synthesized with 75  $\mu\text{M}$   $\text{I}^-$ ; XRD patterns for Cu nanowires, spherical particles, and microplates; TEM image of the side of a Cu microplate; SEM image of the Cu nanocrystals at 30 min taken at 30 kV with a backscatter electron detector; yield of Cu microplates as a function of  $\text{I}^-$  concentration; crystal structure of metal plates reported in previous research; unit cells used for Cu(100) and Cu(111) with corresponding  $k$ -point meshes; and results of convergence tests in terms of the binding energy per hda molecule (in eV) with respect to the  $k$ -point mesh, energy cutoff, and vacuum space (PDF)

## ■ AUTHOR INFORMATION

### Corresponding Authors

**Kristen A. Fichthorn** – Department of Chemical Engineering, The Pennsylvania State University, University Park, Pennsylvania 16802, United States; [orcid.org/0000-0002-4256-714X](https://orcid.org/0000-0002-4256-714X); Email: [fichthorn@psu.edu](mailto:fichthorn@psu.edu)

**Benjamin J. Wiley** – Department of Chemistry, Duke University, Durham, North Carolina 27708, United States; [orcid.org/0000-0002-1314-6223](https://orcid.org/0000-0002-1314-6223); Email: [benjamin.wiley@duke.edu](mailto:benjamin.wiley@duke.edu)

## Authors

**Myung Jun Kim** – Department of Chemistry, Duke University, Durham, North Carolina 27708, United States; Department of Applied Chemistry, Kyung Hee University, Yongin 17104, Republic of Korea; [orcid.org/0000-0002-9056-4904](https://orcid.org/0000-0002-9056-4904)

**Mutya A. Cruz** – Department of Chemistry, Duke University, Durham, North Carolina 27708, United States

**Zihao Chen** – Department of Chemical Engineering, The Pennsylvania State University, University Park, Pennsylvania 16802, United States

**Heng Xu** – Department of Chemistry, Duke University, Durham, North Carolina 27708, United States

**Micah Brown** – Department of Chemistry, Duke University, Durham, North Carolina 27708, United States

Complete contact information is available at:

<https://pubs.acs.org/doi/10.1021/acs.chemmater.0c03596>

## Author Contributions

<sup>||</sup>M.J.K., M.A.C., and Z.C. contributed equally to this manuscript.

## Notes

The authors declare no competing financial interest.

## ■ ACKNOWLEDGMENTS

This work was supported by NSF Grant No. CHE-1808108 (M.J.K., M.A.C., M.B., and B.J.W.) and by the Department of Energy, Office of Basic Energy Sciences, Materials Science Division, DE-FG02-07ER46414 (Z.C. and K.A.F.). Z.C. acknowledges training provided by the Computational Materials Education and Training (CoMET) NSF Research Traineeship (DGE-1449785).

## ■ REFERENCES

- (1) Burda, C.; Chen, X.; Narayanan, R.; El-Sayed, M. A. Chemistry and Properties of Nanocrystals of Different Shapes. *Chem. Rev.* **2005**, *105*, 1025–1102.
- (2) Xie, C.; Niu, Z.; Kim, D.; Li, M.; Yang, P. Surface and Interface Control in Nanoparticle Catalysis. *Chem. Rev.* **2020**, *120*, 1184–1249.
- (3) Wang, C.; Daimon, H.; Lee, Y.; Kim, J.; Sun, S. Synthesis of Monodisperse Pt Nanocubes and Their Enhanced Catalysis for Oxygen Reduction. *J. Am. Chem. Soc.* **2007**, *129*, 6974–6975.
- (4) Wu, J.; Qi, L.; You, H.; Gross, A.; Li, J.; Yang, H. Icosahedral Platinum Alloy Nanocrystals with Enhanced Electrocatalytic Activities. *J. Am. Chem. Soc.* **2012**, *134*, 11880–11883.
- (5) Tsung, C. K.; Kuhn, J. N.; Huang, W.; Aliaga, C.; Hung, L.-I.; Somorjai, G. A.; Yang, P. Sub-10 Nm Platinum Nanocrystals with Size and Shape Control: Catalytic Study for Ethylene and Pyrrole Hydrogenation. *J. Am. Chem. Soc.* **2009**, *131*, 5816–5822.
- (6) Desantis, C. J.; Pevery, A. A.; Peters, D. G.; Skrabalak, S. E. Octopods versus Concave Nanocrystals: Control of Morphology by Manipulating the Kinetics of Seeded Growth via Co-Reduction. *Nano Lett.* **2011**, *11*, 2164–2168.
- (7) Bratlie, K. M.; Lee, H.; Komvopoulos, K.; Yang, P.; Somorjai, G. A. Platinum Nanoparticle Shape Effects on Benzene Hydrogenation Selectivity. *Nano Lett.* **2007**, *7*, 3097–3101.
- (8) Chen, J.; Lim, B.; Lee, E. P.; Xia, Y. Shape-Controlled Synthesis of Platinum Nanocrystals for Catalytic and Electrocatalytic Applications. *Nano Today* **2009**, *4*, 81–95.
- (9) Ye, S.; Rathmell, A. R.; Chen, Z.; Stewart, I. E.; Wiley, B. J. Metal Nanowire Networks: The next Generation of Transparent Conductors. *Adv. Mater.* **2014**, *26*, 6670–6687.
- (10) Niu, Z.; Cui, F.; Kuttner, E.; Xie, C.; Chen, H.; Sun, Y.; Dehestani, A.; Schierle-Armdt, K.; Yang, P. Synthesis of Silver Nanowires with Reduced Diameters Using Benzoin-Derived Radicals

to Make Transparent Conductors with High Transparency and Low Haze. *Nano Lett.* **2018**, *18*, 5329–5334.

(11) Kim, M. J.; Seo, Y.; Cruz, M. A.; Wiley, B. J. Metal Nanowire Felt as a Flow-Through Electrode for High-Productivity Electrochemistry. *ACS Nano* **2019**, *13*, 6998–7009.

(12) Tang, Y.; Gong, S.; Chen, Y.; Yap, L. W.; Cheng, W. Manufacturable Conducting Rubber Ambers and Stretchable Conductors from Copper Nanowire Aerogel Monoliths. *ACS Nano* **2014**, *8*, 5707–5714.

(13) Qian, F.; Lan, P. C.; Freyman, M. C.; Chen, W.; Kou, T.; Olson, T. Y.; Zhu, C.; Worsley, M. A.; Duoss, E. B.; Spadaccini, C. M.; Baumann, T.; Han, T. Y.-J. Ultralight Conductive Silver Nanowire Aerogels. *Nano Lett.* **2017**, *17*, 7171–7176.

(14) Jung, S. M.; Jung, H. Y.; Fang, W.; Dresselhaus, M. S.; Kong, J. A Facile Methodology for the Production of in Situ Inorganic Nanowire Hydrogels/Aerogels. *Nano Lett.* **2014**, *14*, 1810–1817.

(15) Choi, S.; Han, S. I.; Jung, D.; Hwang, H. J.; Lim, C.; Bae, S.; Park, O. K.; Tschabrunn, C. M.; Lee, M.; Bae, S. Y.; Yu, J. W.; Ryu, J. H.; Lee, S.-W.; Park, K.; Kang, P. M.; Lee, W. B.; Nezafat, R.; Hyeon, T.; Kim, D.-H. Highly Conductive, Stretchable and Biocompatible Ag–Au Core–Sheath Nanowire Composite for Wearable and Implantable Bioelectronics. *Nat. Nanotechnol.* **2018**, *13*, 1048–1056.

(16) Catenacci, M. J.; Reyes, C.; Cruz, M. A.; Wiley, B. J. Stretchable Conductive Composites from Cu–Ag Nanowire Felt. *ACS Nano* **2018**, *12*, 3689–3698.

(17) Cruz, M. A.; Ye, S.; Kim, M. J.; Reyes, C.; Yang, F.; Flowers, P. F.; Wiley, B. J. Multigram Synthesis of Cu–Ag Core–Shell Nanowires Enables the Production of a Highly Conductive Polymer Filament for 3D Printing Electronics. *Part. Part. Syst. Charact.* **2018**, *35*, No. 1700385.

(18) Pastoriza-Santos, I.; Liz-Marzán, L. M. Colloidal Silver Nanoplates. State of the Art and Future Challenges. *J. Mater. Chem.* **2008**, *18*, 1724–1737.

(19) Chen, M.; Tang, S.; Guo, Z.; Wang, X.; Mo, S.; Huang, X.; Liu, G.; Zheng, N. Core–Shell Pd@Au Nanoplates as Theranostic Agents for in-Vivo Photoacoustic Imaging, CT Imaging, and Photothermal Therapy. *Adv. Mater.* **2014**, *26*, 8210–8216.

(20) Gao, C.; Lu, Z.; Liu, Y.; Zhang, Q.; Chi, M.; Cheng, Q.; Yin, Y. Highly Stable Silver Nanoplates for Surface Plasmon Resonance Biosensing. *Angew. Chem., Int. Ed.* **2012**, *51*, 5629–5633.

(21) Homan, K. A.; Souza, M.; Truby, R.; Luke, G. P.; Green, C.; Vreeland, E.; Emelianov, S. Silver Nanoplate Contrast Agents for in Vivo Molecular Photoacoustic Imaging. *ACS Nano* **2012**, *6*, 641–650.

(22) Li, R.-Z.; Hu, A.; Bridges, D.; Zhang, T.; Oakes, K. D.; Peng, R.; Tumuluri, U.; Wu, Z.; Feng, Z. Robust Ag Nanoplate Ink for Flexible Electronics Packaging. *Nanoscale* **2015**, *7*, 7368–7377.

(23) Lee, J.-W.; Han, J.; Lee, D. S.; Bae, S.; Lee, S. H.; Lee, S.-K.; Moon, B. J.; Choi, C.-J.; Wang, G.; Kim, T.-W. 2D Single-Crystalline Copper Nanoplates as a Conductive Filler for Electronic Ink Applications. *Small* **2018**, *14*, No. 1703312.

(24) Stewart, I. E.; Kim, M. J.; Wiley, B. J. Effect of Morphology on the Electrical Resistivity of Silver Nanostructure Films. *ACS Appl. Mater. Interfaces* **2017**, *9*, 1870–1879.

(25) Audoit, J.; Laffont, L.; Lonjon, A.; Dantras, E.; Lacabanne, C. Percolative Silver Nanoplates/PVDF Nanocomposites: Bulk and Surface Electrical Conduction. *Polymer* **2015**, *78*, 104–110.

(26) Burrows, N. D.; Vartanian, A. M.; Abadeer, N. S.; Grzincic, E. M.; Jacob, L. M.; Lin, W.; Li, J.; Dennison, J. M.; Hinman, J. G.; Murphy, C. J. Anisotropic Nanoparticles and Anisotropic Surface Chemistry. *J. Phys. Chem. Lett.* **2016**, *7*, 632–641.

(27) Grzelczak, M.; Pérez-Juste, J.; Mulvaney, P.; Liz-Marzán, L. M. Shape Control in Gold Nanoparticle Synthesis. *Chem. Soc. Rev.* **2008**, *37*, 1783–1791.

(28) Tao, A. R.; Habas, S.; Yang, P. Shape Control of Colloidal Metal Nanocrystals. *Small* **2008**, *4*, 310–325.

(29) Huo, D.; Kim, M. J.; Lyu, Z.; Shi, Y.; Wiley, B. J.; Xia, Y. One-Dimensional Metal Nanostructures: From Colloidal Syntheses to Applications. *Chem. Rev.* **2019**, *119*, 8972–9073.

(30) Walsh, M. J.; Tong, W.; Katz-Boon, H.; Mulvaney, P.; Etheridge, J.; Funston, A. M. A Mechanism for Symmetry Breaking and Shape Control in Single-Crystal Gold Nanorods. *Acc. Chem. Res.* **2017**, *50*, 2925–2935.

(31) Xia, Y.; Xia, X.; Peng, H.-C. Shape-Controlled Synthesis of Colloidal Metal Nanocrystals: Thermodynamic versus Kinetic Products. *J. Am. Chem. Soc.* **2015**, *137*, 7947–7966.

(32) Chen, Z.; Chang, J. W.; Balasanthiran, C.; Milner, S. T.; Rioux, R. M. Anisotropic Growth of Silver Nanoparticles Is Kinetically Controlled by Polyvinylpyrrolidone Binding. *J. Am. Chem. Soc.* **2019**, *141*, 4328–4337.

(33) Qi, X.; Balankura, T.; Fichthorn, K. A. Theoretical Perspectives on the Influence of Solution-Phase Additives in Shape-Controlled Nanocrystal Synthesis. *J. Phys. Chem. C* **2018**, *122*, 18785–18794.

(34) Qi, X.; Fichthorn, K. A. Theory of the Thermodynamic Influence of Solution-Phase Additives in Shape-Controlled Nanocrystal Synthesis. *Nanoscale* **2017**, *9*, 15635–15642.

(35) Xia, Y.; Xiong, Y.; Lim, B.; Skrabalak, S. E. Shape-Controlled Synthesis of Metal Nanocrystals: Simple Chemistry Meets Complex Physics? *Angew. Chem., Int. Ed.* **2009**, *48*, 60–103.

(36) Kim, M. J.; Flowers, P. F.; Stewart, I. E.; Ye, S.; Baek, S.; Kim, J. J.; Wiley, B. J. Ethylenediamine Promotes Cu Nanowire Growth by Inhibiting Oxidation of Cu(111). *J. Am. Chem. Soc.* **2017**, *139*, 277–284.

(37) Kim, M. J.; Alvarez, S.; Chen, Z.; Fichthorn, K. A.; Wiley, B. J. Single-Crystal Electrochemistry Reveals Why Metal Nanowires Grow. *J. Am. Chem. Soc.* **2018**, *140*, 14740–14746.

(38) Kim, M. J.; Brown, M.; Wiley, B. J. Electrochemical Investigations of Metal Nanostructure Growth with Single Crystals. *Nanoscale* **2019**, *11*, 21709–21723.

(39) Kim, M. J.; Alvarez, S.; Yan, T.; Tadepalli, V.; Fichthorn, K. A.; Wiley, B. J. Modulating the Growth Rate, Aspect Ratio, and Yield of Copper Nanowires with Alkylamines. *Chem. Mater.* **2018**, *30*, 2809–2818.

(40) Liu, S.-H.; Fichthorn, K. A. Interaction of Alkylamines with Cu Surfaces: A Metal–Organic Many-Body Force Field. *J. Phys. Chem. C* **2017**, *121*, 22531–22541.

(41) Liu, S.-H.; Balankura, T.; Fichthorn, K. A. Self-Assembled Monolayer Structures of Hexadecylamine on Cu Surfaces: Density-Functional Theory. *Phys. Chem. Chem. Phys.* **2016**, *18*, 32753–32761.

(42) Kirkland, A. I.; Jefferson, D. A.; Duff, D. G.; Edwards, P. P.; Gameson, I.; Johnson, B. F. G.; Smith, D. J. Structural Studies of Trigonal Lamellar Particles of Gold and Silver. *Proc. R. Soc. London, Ser. A* **1993**, *440*, 589–609.

(43) Castaño, V.; Gómez, A.; Jose Yacaman, M. Microdiffraction and Surface Structure of Small Gold Particles. *Surf. Sci.* **1984**, *146*, L587–L592.

(44) Tanaka, N.; Cowley, J. M. Studies of Planar Defects in Silver Plate-like Crystals by CBED and HRTEM Techniques. *MRS Proc.* **1985**, *41*, No. 155.

(45) Lofton, C.; Sigmund, W. Mechanisms Controlling Crystal Habits of Gold and Silver Colloids. *Adv. Funct. Mater.* **2005**, *15*, 1197–1208.

(46) Aherne, D.; Ledwith, D. M.; Gara, M.; Kelly, J. M. Optical Properties and Growth Aspects of Silver Nanoprisms Produced by a Highly Reproducible and Rapid Synthesis at Room Temperature. *Adv. Funct. Mater.* **2008**, *18*, 2005–2016.

(47) Yu, T.; Wu, Z.; Kim, W.-S. Mild Temperature Synthesis of Gold Nanoplates Using Polyethyleneimine and Their Improved Surface Enhanced Raman Signal. *RSC Adv.* **2014**, *4*, 37516–37521.

(48) Golze, S. D.; Hughes, R. A.; Rouvimov, S.; Neal, R. D.; Demille, T. B.; Neretina, S. Plasmon-Mediated Synthesis of Periodic Arrays of Gold Nanoplates Using Substrate-Immobilized Seeds Lined with Planar Defects. *Nano Lett.* **2019**, *19*, 5653–5660.

(49) Goebel, J.; Zhang, Q.; He, L.; Yin, Y. Monitoring the Shape Evolution of Silver Nanoplates: A Marker Study. *Angew. Chem., Int. Ed.* **2012**, *51*, 552–555.

(50) Kim, M. H.; Kwak, S. K.; Im, S. H.; Lee, J.-B.; Choi, K.-Y.; Byun, D.-J. Maneuvering the Growth of Silver Nanoplates: Use of

Halide Ions to Promote Vertical Growth. *J. Mater. Chem. C* **2014**, *2*, 6165–6170.

(51) Curtis, A. C.; Duff, D. G.; Edwards, P. P.; Jefferson, D. A.; Johnson, B. F. G.; Kirkland, A. I.; Wallace, A. S. Preparation and Structural Characterization of an Unprotected Copper Sol. *J. Phys. Chem. A* **1988**, *92*, 2270–2275.

(52) Zeng, J.; Xia, X.; Rycenga, M.; Henneghan, P.; Li, Q.; Xia, Y. Successive Deposition of Silver on Silver Nanoplates: Lateral versus Vertical Growth. *Angew. Chem., Int. Ed.* **2011**, *50*, 244–249.

(53) Bindra, P.; Roldan, J. Mechanisms of Electroless Metal Plating. III. Mixed Potential Theory and the Interdependence of Partial Reactions. *J. Appl. Electrochem.* **1987**, *17*, 1254–1266.

(54) Feldman, B. J.; Melroy, O. R. The Mechanism of Electroless Cu Deposition: Extraction of the Oxidative and Reductive Electrochemical Half-Cell Currents from a Complete Bath. *J. Electrochem. Soc.* **1989**, *136*, 640–643.

(55) Yanson, Y. I.; Rost, M. J. Structural Accelerating Effect of Chloride on Copper Electrodeposition. *Angew. Chem., Int. Ed.* **2013**, *52*, 2454–2458.

(56) Kim, M. J.; Kim, H. C.; Kim, J. J. The Influences of Iodide Ion on Cu Electrodeposition and TSV Filling. *J. Electrochem. Soc.* **2016**, *163*, D434–D441.

(57) Huemann, S.; Hai, N. T. M.; Broekmann, P.; Wandelt, K.; Zajonz, H.; Dosch, H.; Renner, F. X-Ray Diffraction and STM Study of Reactive Surfaces under Electrochemical Control: Cl and I on Cu(100). *J. Phys. Chem. B* **2006**, *110*, 24955–24963.

(58) McCrum, I. T.; Akhade, S. A.; Janik, M. J. Electrochemical Specific Adsorption of Halides on Cu 111,100, and 211: A Density Functional Theory Study. *Electrochim. Acta* **2015**, *173*, 302–309.

(59) Nørskov, J. K.; Rossmeisl, J.; Logadottir, A.; Lindqvist, L.; Kitchin, J. R.; Bligaard, T.; Jónsson, H. Origin of the Overpotential for Oxygen Reduction at a Fuel-Cell Cathode. *J. Phys. Chem. B* **2004**, *108*, 17886–17892.

(60) Kresse, G.; Hafner, J. Ab-Initio Molecular-Dynamics for Liquid-Metals. *Phys. Rev. B* **1993**, *47*, 558–561.

(61) Kresse, G.; Hafner, J. Ab Initio Molecular-Dynamics Simulation of the Liquid-Metal-Amorphous-Semiconductor Transition in Germanium. *Phys. Rev. B* **1994**, *49*, 14251–14269.

(62) Kresse, G.; Furthmüller, J. Efficient Iterative Schemes for Ab Initio Total-Energy Calculations Using a Plane-Wave Basis Set. *Phys. Rev. B* **1996**, *54*, 11169–11186.

(63) Reuter, K.; Scheffler, M. Composition, Structure, and Stability of RuO<sub>2</sub>(110) as a Function of Oxygen Pressure. *Phys. Rev. B* **2001**, *65*, No. 35406.

(64) Fichthorn, K. A.; Chen, Z. Surface Science of Shape-Selective Metal Nanocrystal Synthesis from First-Principles: Growth of Cu Nanowires and Nanocubes. *J. Vac. Sci. Technol., A* **2020**, *38*, No. 23210.

(65) Gossenberger, F.; Roman, T.; Groß, A. Equilibrium Coverage of Halides on Metal Electrodes. *Surf. Sci.* **2015**, *631*, 17–22.

(66) Bratsch, S. G. Standard Electrode Potentials and Temperature Coefficients in Water at 298.15 K. *J. Phys. Chem. Ref. Data* **1989**, *18*, 1–21.

(67) Atkins, P. W.; De Paula, J.; Keeler, J. *Atkins' Physical Chemistry*, 11th ed.; Oxford University Press, 2018.

(68) Qi, X.; Chen, Z.; Yan, T.; Fichthorn, K. A. Growth Mechanism of Five-Fold Twinned Ag Nanowires from Multiscale Theory and Simulations. *ACS Nano* **2019**, *13*, 4647–4656.

(69) Blöchl, P. E. Projector Augmented-Wave Method. *Phys. Rev. B* **1994**, *50*, 17953–17979.

(70) Kresse, G.; Joubert, D. From Ultrasoft Pseudopotentials to the Projector Augmented-Wave Method. *Phys. Rev. B* **1999**, *59*, 1758–1775.

(71) Perdew, J. P.; Burke, K.; Ernzerhof, M. Generalized Gradient Approximation Made Simple. *Phys. Rev. Lett.* **1996**, *77*, 3865–3868.